Low-temperature magnetic, galvanomagnetic, and thermoelectric properties of the type-I clathrates Ba8NixSi46–x

Christophe Candolfi, Umut Aydemir, Alim Ormeci, Michael Baitinger, Niels Oeschler, Franck Steglich, Yuri Grin

Low-temperature magnetic, galvanomagnetic, and thermoelectric properties of the type-I clathrates $Ba_8Ni_xSi_{46-x}$

C. Candolfi,* U. Aydemir, A. Ormeci,† M. Baitinger, N. Oeschler, F. Steglich, and Yu. Grin
Max-Planck-Institut für Chemische Physik fester Stoffe, Nöthnitzer Str. 40, D-01187 Dresden, Germany
(Received 26 January 2011; revised manuscript received 3 March 2011; published 4 May 2011)

Galvanomagnetic and thermoelectric properties including Hall effect, electrical resistivity, thermopower, and thermal conductivity of polycrystalline type-I clathrates $Ba_8Ni_xSi_{46-x}$ ($2.6 \leqslant x \leqslant 3.8$) have been studied in the 2- to 350-K temperature range. Further characterization of the electronic properties of these compounds has been performed via low-temperature specific heat and magnetic susceptibility measurements (2–300 K). The electronic band structure, density of states, dispersion curves, and Fermi surface were calculated within the full-potential local-orbital method (FPLO). These calculations have not only revealed that the electronic band structure evolves in a nonrigid manner but have also shown that the density of states at the Fermi level strongly varies with x. The variations in the band structure have been experimentally confirmed by transport properties and specific heat measurements. Regardless of the Ni content, the Fermi surface shows disconnected electron and hole sections that appear consistent with thermopower data indicating that both types of carriers contribute to the electrical conduction in these materials. Magnetic susceptibility measurements have indicated that the Ni atoms do not carry any magnetic moment in these compounds. All the investigated samples exhibit metallic-like behavior resulting in moderate thermopower values and thus, in low dimensionless thermoelectric figures of merit ZT.

DOI: 10.1103/PhysRevB.83.205102 PACS number(s): 82.75.−z, 72.15.−v

I. INTRODUCTION

Intermetallic clathrates have received increasing attention over the last decades due to their intriguing properties such as superconductivity in sp^3 framework, magnetic ordering, glass-like thermal conductivity, mechanical properties, or high thermoelectric efficiency.[1–3] The possibility of finely tuning the electronic properties from metallic-like to semiconducting-like behavior coupled with a cage-like crystalline structure that may efficiently disrupt the harmonic modes of the lattice are key ingredients to achieving attractive thermoelectric properties. The necessity of meeting these requirements is captured in the dimensionless figure of merit defined as $ZT = \alpha^2 T/\rho\lambda$ where α is the thermopower or Seebeck coefficient, ρ is the electrical resistivity, λ is the total thermal conductivity, and T is the absolute temperature.[4]

Synonymous with high thermoelectric efficiency, high ZT values were discovered in clathrates crystallizing in the so-called type-I structure and based on a Ge framework.[5,6] The crystal structure of type-I clathrates is composed of a three-dimensional arrangement of large polyhedral cages (20-atom pentagon dodecahedron and 24-atom tetrakaidecahedron; Fig. 1 in green and blue, respectively) built by "host" atoms in which the "guest" atoms are encapsulated. Clathrates can be classified according to the formal charge of the framework (e.g., polyanionic or polycationic).[7] If the framework bears a negative charge (composed of group 14 elements such as Si, Ge, or Sn) with respect to the guest atoms such as alkali metals (Na, K, Rb, Cs), alkaline-earth (Ba, Sr), or the rare-earth Eu,[1,7] then the resulting structure is referred as polyanionic clathrates. On the other hand, if the framework bears a positive charge, then polycationic clathrates form with anions as guest atoms such as Te, Cl, Br, or I.[7–9] In polyanionic clathrates, the framework atoms can be partially substituted by group 13 elements or transition metals. Strong efforts were devoted to further explore this family of materials, namely the parent $Ba_8Ge_{43}\square_3$ (□ stands for a vacancy) compound and its ternary derivatives $Ba_8M_xGe_{46-x-y}\square_y$ (where M = Ga, In, Al, Pd, Pt, Ni, Au, etc.).[10–15]

A widespread use of thermoelectric generators based on clathrate compounds would require both n- and p-type materials being of equal thermoelectric potential and compatible in terms of thermal expansion to minimize stress effects and enhance their chemical compatibility within the module. However, even though several clathrates have been discovered to exhibit either a p-type electrical conduction such as $Ba_8Ga_{16}Ge_{30}$, $Ba_8Ga_{16}Zn_xGe_{30-x}$, and $Ba_8Ga_{16}Al_xGe_{30-x}$, or a transition from n-type to p-type conduction such as $Ba_8Au_xGe_{46-x-y}\square_y$ and $Ba_8Ni_xGe_{46-x-y}\square_y$,[15–22] most of the clathrates studied so far are characterized by an n-type behavior. In addition, the ZT values of the available p-type clathrates remain lower than their n-type counterparts.

A p-type behavior is, however, not restricted to the Ge-based type-I clathrates and has also been reported in the Si-based analogs.[22] A transition from n-type to p-type has been unveiled in $Ba_8Au_xSi_{46-x}$, a feature shared by the $Ba_8Au_xGe_{46-x-y}\square_y$ compounds.[23] Even though the number of studies carried out on the Ge-based clathrates greatly exceeds that undertaken on the Si-based clathrates, several investigations on the transport properties of the $Ba_8M_xSi_{46-x}$ compounds (M = Ga, Al, Pd, Pt, Zn, and Cd) were recently reported.[24–29] Electronic band structure calculations have shown that substituting on the Si framework with transition metals generally leads to metallic-like behavior that is detrimental to achieving desirable thermoelectric properties.[30–32] These theoretical findings were experimentally confirmed by low-temperature transport properties performed on the Pd, Pt, Zn, and Cd-substituted compounds.[28,29] However, semiconducting properties develop in the $Ba_8Ga_xSi_{46-x}$ system for $x \sim 16$, paving the way to finely tune both the electrical resistivity and thermopower.[24–26] So far, the $Ba_8Ga_{16}Si_{30}$ compound exhibits the highest ZT value discovered in Si-based type-I clathrates ($ZT \sim 0.8$ at 1000 K).[24,25] Interestingly, this value is comparable to that obtained in the Ge-based analog and shows that replacing Ge

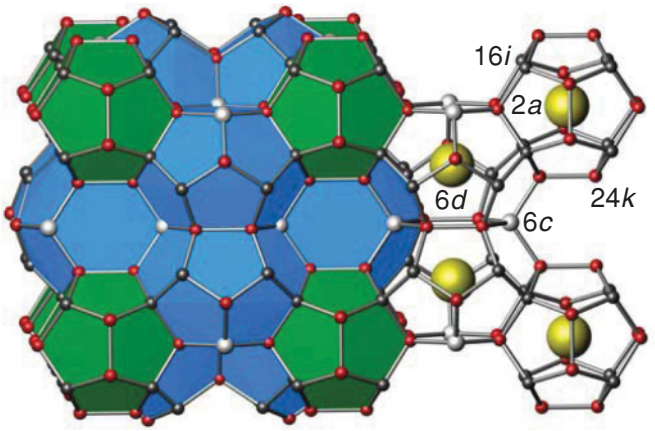

FIG. 1. (Color online) Crystal structure of the type-I clathrate. The framework atoms are located at the 6*c* (white), 16*i* (gray), and 24*k* (red) sites while the "guest" atoms are located at the 2*a* and 6*d* (yellow) sites.

by Si may be a worthwhile line of research to pursue.[4] In addition, extending these studies of the transport properties at low temperatures may provide valuable insights into the scattering mechanisms of the charge carriers, a key information in controlling and optimizing the thermoelectric properties of these materials. Hence, new *p*-type clathrate compounds with enhanced thermoelectric properties may be discovered. In this regard, the similar behavior of the Au-containing clathrates raises the question whether the *n*- to *p*-type transition observed in $Ba_8Ni_xGe_{46-x-y}\square_y$ may also occur in the Si-based compounds.

Here, we report a joint theoretical and experimental investigation of the low-temperature transport properties of polycrystalline $Ba_8Ni_xSi_{46-x}$ clathrates ($2.6 \leqslant x \leqslant 3.8$) through first-principles calculations and thermoelectric, galvanomagnetic, and magnetic properties measurements. The variations in the electronic band structure with the Ni content, the magnetic state of the Ni atoms as well as the influence of this substitution on the thermoelectric properties stand for the main issues we address in the present study.

II. EXPERIMENTAL AND COMPUTATIONAL DETAILS

Polycrystalline $Ba_8Ni_xSi_{46-x}$ samples with nominal Ni content of $x = 2.5$, 2.65, 2.75, 2.85, 3.0, 3.5, and 4.0 were synthesized from crystalline Ba pieces (ChemPur, 99.9% metal basis), Ni powder (Chempur, 99.9% metal basis), and Si pieces (ChemPur, 99.9999%) in an argon-filled glove box (O_2 and $H_2O \leqslant 1$ ppm). Stoichiometric amounts of the elements placed in glassy carbon crucibles were slowly heated in an induction furnace until a complete melt was achieved and then cooled down to room temperature. To ensure a good chemical homogeneity, all the ingots were further annealed for one week at 1000 °C in glassy carbon crucibles sealed in tantalum tubes. These tubes, which were in turn sealed in argon-filled quartz ampoules, were finally quenched in water.

Structural and chemical characterizations were performed through powder x-ray diffraction (PXRD), single crystal x-ray diffraction, differential scanning calorimetry (DSC), energy dispersive x-ray spectroscopy (EDXS), and wavelength dispersive x-ray spectroscopy (WDXS). The lattice parameters were refined from PXRD data using LaB_6 [$a = 4.15683(9)$ Å at 295 K] as an internal standard with the WinCSD program package.[33] The details of these crystallographic investigations will be presented elsewhere.[34]

For transport property measurements, bar-shaped samples were cut from the annealed ingots into typical dimensions of $2 \times 2 \times 6$ mm^3 with a diamond-wire saw. Thermoelectric properties including electrical resistivity, thermopower, and thermal conductivity were simultaneously measured using the thermal transport option of a physical property measurement system (PPMS-Quantum Design) in the 5- to 350-K temperature range. Hall effect measurements were carried out with a PPMS over the 10- to 300-K temperature range and under magnetic fields ranging from −5 to 5 T. A five-point method using copper wires attached onto the sample with a tiny amount of silver paste was used. Magnetic susceptibility was measured in the 2- to 300-K temperature range using a MPMS SQUID magnetometer (Quantum Design) under a magnetic field of 1 T. Specific heat measurements under zero magnetic field were performed with a PPMS by a standard relaxation method between 1.9 and 15 K.

Electronic band structure calculations of $Ba_8Ni_xSi_{46-x}$ ($x = 0$, 2.0, 3.0, 4.0, and 6.0) were carried out by the all-electron, full-potential local orbital (FPLO) method.[35] The self-consistent crystal potential was constructed within the local density approximation (LDA) applying the Perdew-Wang parameterization for the exchange-correlation part.[36] The two end-member compounds, $x = 0$ and 6, display an ordered crystal structure enabling one to use the original space group *Pm*-3*n* (for $x = 6$, Ni atoms fully occupy the 6*c* position). However, to treat the chemical disorder which inevitably accompanies a chemical substitution at the 6*c* position, a supercell approach is required for the other cases ($x = 2$, 3, and 4). Supercells were chosen by taking into account the group-subgroup relations along with the way the 6*c* Wyckoff position in *Pm*-3*n* is split in possible subgroups. Consequently, for $x = 2$ and 4, the space group $P4_122$ (No. 91) with lattice parameters $a \times a \times 2a$ containing two formula units was used, whereas for $x = 3$ the calculations were conducted in the space group *Ia*-3*d* (No. 230) with lattice parameters $2a \times 2a \times 2a$ (four formula units in the primitive cell). In all the present calculations, Ba atoms were assumed to be located at the centers of the cages and the possibility of

TABLE I. Crystallographic data of the $x = 2.6$, 3.2, and 3.7 compounds derived from single-crystal x-ray diffraction experiments.

Actual Ni content *x*	*a* (Å)	Si in 16*i* (*x*, *x*, *x*)	Si in 24*k* (0, *y*, *z*)
2.6	10.2982	0.18463	$y = 0.31126$ $z = 0.12137$
3.2	10.2922	0.18442	$y = 0.31233$ $z = 0.12178$
3.7	10.2906	0.18440	$y = 0.31249$ $z = 0.12165$

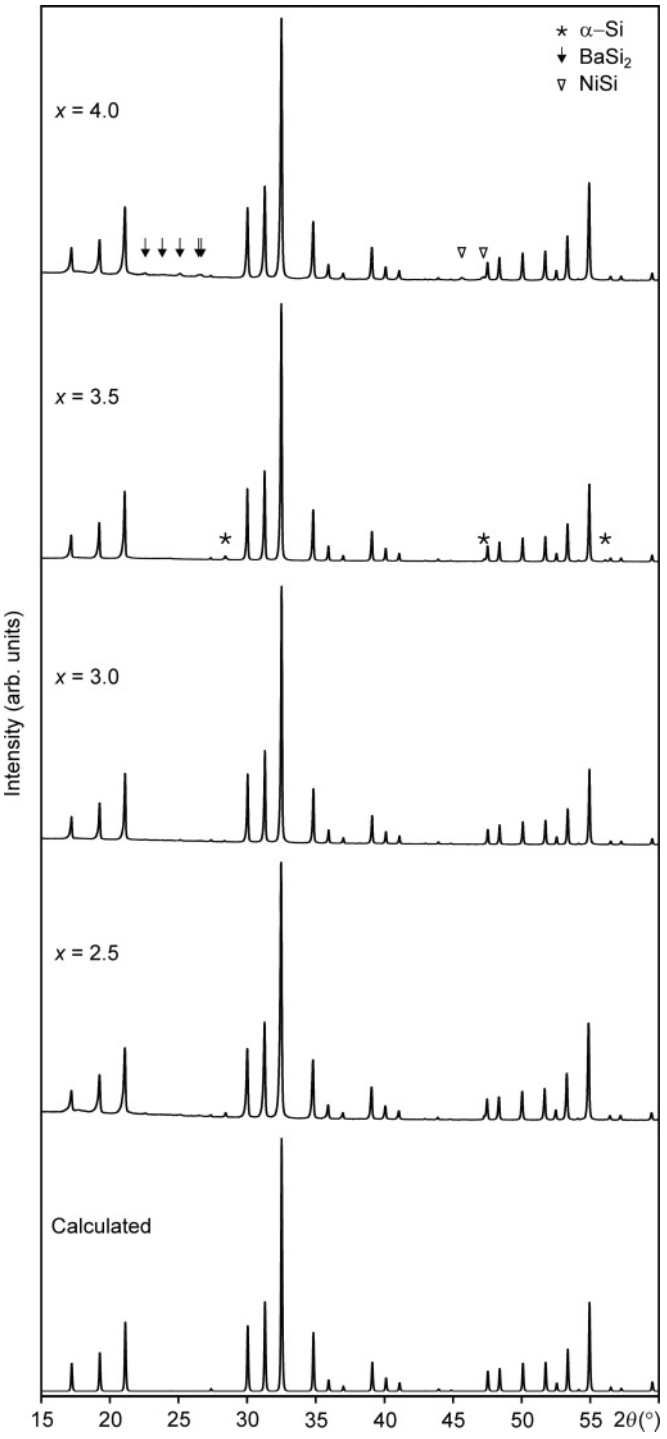

FIG. 2. PXRD patterns of $Ba_8Ni_xSi_{46-x}$ samples of nominal compositions $x = 2.5$, 3.0, 3.5, and 4.0 together with the calculated profile based on a single crystal analysis for $x = 3.0$ (Ref. 34). The symbols mark the position of the reflections originating from the secondary phases (only shown for $x = 3.5$ and 4.0).

vacancies at the 6*c* position was ignored. The good qualitative agreement found between the experimental and theoretical results (see following sections) suggests that the qualitative picture emerging from the first-principles calculations will not change significantly by the introduction of vacancies. Nonetheless, the effects of vacancies on the electronic structure especially for the $x = 4$ case will be discussed in a separate study.[34] Regarding the binary clathrate Ba_8Si_{46}, only the unit cell volume was optimized while keeping the experimental values of the atomic coordinates fixed.[37] Since the $x = 6$ clathrate does not exist, to the best of our knowledge, both the atomic coordinates and the unit cell volume were optimized. In the case of $x = 2$, 3, and 4, the experimental crystallographic parameters derived from x-ray diffraction data for $x = 2.6$, 3.2, and 3.7, respectively, were used (Table I).[34]

III. RESULTS AND DISCUSSION

A. Structural and chemical characterizations

Based on the WDXS and PXRD results, the homogeneity range of $Ba_8Ni_xSi_{46-x}$ was determined to be $2.4 \leqslant x \leqslant 3.8$ at 1000 °C. Below $x = 2.4$, $BaSi_2$ and Si are present together with the clathrate-I phase. Note that clathrate phases exhibiting lower Ni contents ($x < 2.4$) were achieved as a minority phase in a mixture of $BaSi_2$ and α-Si by fast cooling.[34] Clathrates with higher Ni contents than $x = 3.8$ could not be obtained and these samples contain increasing amounts of NiSi and $NiSi_2$ as secondary phases. For samples in the homogeneity range, EDXS and WDXS analyses have revealed a very good chemical homogeneity and correlation between the nominal and actual compositions and confirmed the presence of small amounts of secondary phases. The average grain size estimated from scanning electron microscopy (SEM) images was found to be ~200 μm. The nominal and actual compositions as obtained from WDXS experiments and the nature of the secondary phases detected together with the lattice parameters are summarized in Table II. We shall use the actual Ni content hereafter.

Both PXRD and single crystal studies have shown that all samples crystallize in the cubic type-I clathrate structure with space group *Pm*-3*n* (No. 223). In addition, PXRD experiments have shown that, in the above-mentioned homogeneity range, the samples only exhibit a very small amount of secondary phases (Fig. 2). Ideally, Ba1 and Ba2 atoms are located at the centers of the 20-atom cage, 2*a* (0, 0, 0), and at the centers of the 24-atom cage, 6*d* ($\frac{1}{4}$, $\frac{1}{2}$, 0), respectively. In accordance with the results of prior studies on various $Ba_8M_xE_{46-x}$ clathrates (M = transition metal and E = Si, Ge) the 6*c* ($\frac{1}{4}$, 0, $\frac{1}{2}$) site was found to be occupied by both Ni and Si atoms (Ni1 and Si1) giving rise to chemical disorder. The remaining Si atoms (Si2 and Si3) are located at 16*i* (x, x, x), and 24*k* (0, y, z) positions, respectively.[34] Rietveld refinements and single crystal x-ray diffraction data analyses have demonstrated that the Ba sites are fully occupied. Therefore, the chemical compositions were determined considering 8 Ba atoms per formula unit. In addition, these measurements have revealed that the 6*c* site is fully occupied for $x < 3.1$ whereas at higher Ni contents, our data suggest the presence of vacancies on this site (up to 0.8 vacancies per formula unit at $x = 3.8$).[34] Similar vacancy formation in the Si framework was also reported for $Ba_8Al_{14}Si_{31}$.[27] As shown in Fig. 3, the lattice parameter, a, sharply decreases with the Ni content up to $x \approx 3$ before exhibiting a smoother decrease up to $x = 3.8$. Powder and single crystal x-ray diffraction experiments have shown

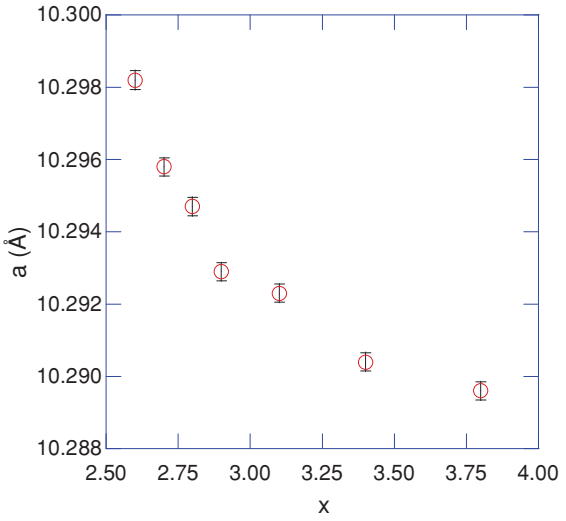

FIG. 3. (Color online) Lattice parameter of $Ba_8Ni_xSi_{46-x}$, a, as a function of the actual Ni concentration.

that the Ni1-Si3 interatomic distances ($d_{Ni1-Si3} \approx 2.34$ Å) are slightly shorter than the Si1-Si3 bond length in Ba_8Si_{46} [$d_{Si1-Si3} \approx 2.42$ Å, $a = 10.328(2)$ Å] [37] thereby leading to an overall decrease of the lattice parameter with increasing Ni content. To have a deeper insight into the variations in the transport properties arising from the decrease of a, four samples falling into the $2.5 < x < 3.0$ compositional range were subsequently studied.

B. Electronic band structure calculations

As mentioned in a preceding section, the use of supercells is required to investigate the electronic structures of the $Ba_8Ni_xSi_{46-x}$ clathrates for $x = 2$, 3, 4. In the tetragonal space group $P4_122$, suitable for $x = 2$ and 4, the 6*c* position of *Pm*-3*n* splits into three Wyckoff positions: two 4*a* (0, *y*, 0) positions (one with $y = \frac{1}{4}$, the other with $y = -\frac{1}{4}$) and the 4*c* (*x*, *x*, 3/8) position (with $x = \frac{1}{2}$). Two distinct models are then possible: The 4*a* sites can be occupied either by the atoms of (a) the same element or by (b) both Ni and Si. The latter model has a lower total energy, the energy differences amounting to 2.4 and 2.3 meV atom^{-1} for $x = 2$ and 4, respectively. For $x = 3$, the 6*c* position in *Pm*-3*n* splits into 24*c* (1/8 , 0, $\frac{1}{4}$) and 24*d* (3/8, 0, $\frac{1}{4}$) positions in the space group *Ia*-3*d*. The total energy difference between the Ni-at-24*c* and the Ni-at-24*d* models is quite small, 0.5 meV atom^{-1} in favor of the former. This slight difference may be regarded as a sign of lack of superstructure.

TABLE III. Total and atom-resolved densities of states at the Fermi level expressed in states eV^{-1} (f.u.)$^{-1}$

Theoretical Ni content x	0	2.0	3.0	4.0	6.0
$N(E_F)$	34.66	35.83	9.89	16.81	22.76
Ba	7.79	7.06	1.96	2.28	1.82
Si at 6*c*	4.09	3.61	0.66	0.51	/
Si at 16*i*	7.38	8.04	2.52	3.73	4.42
Si at 24*k*	15.40	16.06	4.12	7.24	11.39
Ni at 6*c*	/	1.06	0.63	3.04	5.13

The electronic band structures of $Ba_8Ni_xSi_{46-x}$ for $x = 0$, 2, 3, and 4 are shown in Fig. 4. Note that, except for the binary compound, the Brillouin zones shown are not folded back to that of the original cubic lattice but are those of the supercell lattices. The number of bands crossing the Fermi level amounts to four for $x = 0$ and 2, then increases to eight for $x = 3$ before decreasing to only three bands for $x = 4$. This first result highlights the sensitivity of the electronic structure of these compounds to the Ni content and thus indicates a nonrigid-like evolution of the band structure with x. The higher degree of complexity of the band structure in the $x = 3$ compound may also support the possibility of distinct transport properties that may extend over a small concentration range around $x = 3.0$.

Regardless of the Ni content, the Fermi surfaces exhibit common features that we now discuss for the illustrative $x = 4$ case (Fig. 5). The Fermi surface of the lowest-energy band, shown in Fig. 5(a), consists of three hole-like objects. A large "pulley-like" surface is centered at the Γ point and contains relatively slow hole-like carriers (note that the *Z* point is barely excluded). The Fermi surface around the *X* point contains both slow (mostly those with **k** vectors closer to Γ) and fast (mostly those with **k** vectors closer to *M*) holes. The hole pocket around the *M* point has the smallest area and the **k** vectors of its fastest holes are closer to the Γ point. Because of the symmetry, the bands are degenerate on the top surface of the Brillouin zone. The Fermi surfaces due to the two higher energy bands are all electron-like [Figs. 5(b) and 5(c)]. Although the Fermi surface due to the third band [Fig. 5(c)] is simple, the picture is more complicated for the second band [Fig. 5(b)]. The Fermi surface around the *A*

TABLE II. WDXS compositions, nature of the secondary phases, and lattice parameters (a) of $Ba_8Ni_xSi_{46-x}$. The total amount of secondary phases was estimated to be less than 2–3 wt% for all compositions.

Nominal composition	WDXS	Secondary phases	a (Å)
$Ba_8Ni_{2.5}Si_{43.5}$	$Ba_8Ni_{2.6(1)}Si_{42.6(1)}$	$BaSi_2$ and $\alpha-Si$	10.2982(1)
$Ba_8Ni_{2.65}Si_{43.35}$	$Ba_8Ni_{2.7(1)}Si_{42.9(1)}$	$BaSi_2$ and $\alpha-Si$	10.2958(1)
$Ba_8Ni_{2.75}Si_{43.25}$	$Ba_8Ni_{2.8(1)}Si_{42.6(1)}$	$BaSi_2$ and $\alpha-Si$	10.2947(1)
$Ba_8Ni_{2.85}Si_{43.35}$	$Ba_8Ni_{2.9(1)}Si_{42.5(1)}$	$BaSi_2$ and $\alpha-Si$	10.2929(1)
$Ba_8Ni_3Si_{43}$	$Ba_8Ni_{3.1(1)}Si_{42.3(1)}$	$BaSi_2$ and $\alpha-Si$	10.2923(1)
$Ba_8Ni_{3.5}Si_{42.5}$	$Ba_8Ni_{3.4(1)}Si_{42.4(1)}$	$\alpha-Si$	10.2904(1)
$Ba_8Ni_4Si_{42}$	$Ba_8Ni_{3.8(1)}Si_{41.3(1)}$	$BaSi_2$, NiSi and $NiSi_2$	10.2896(1)

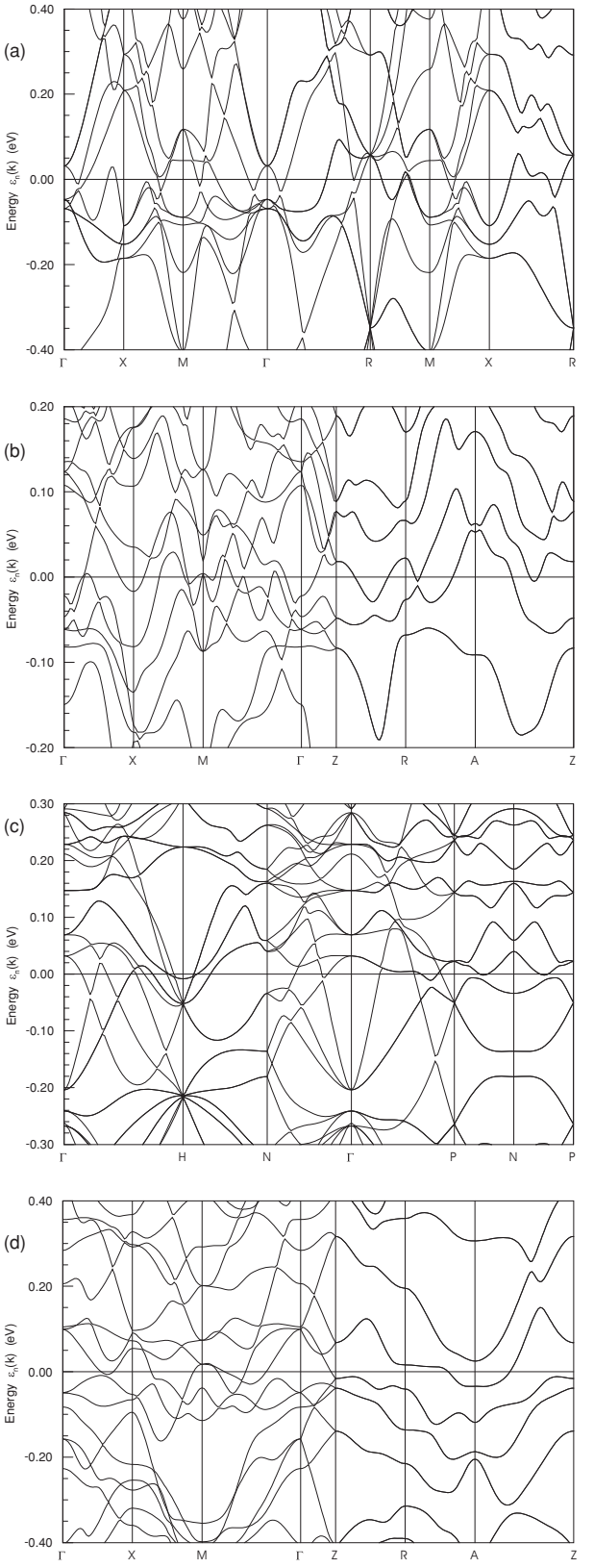

FIG. 4. Dispersion curves along high symmetry directions near the Fermi level of $Ba_8Ni_xSi_{46-x}$ for $x = 2$, 3, and 4.

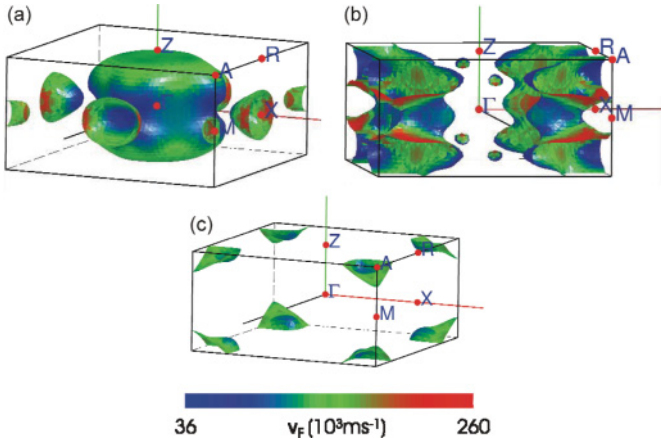

FIG. 5. (Color online) Fermi surface of $Ba_8Ni_xSi_{46-x}$ for $x = 4$. The shading is by Fermi velocity.

point, similar to that in Fig. 5(c), combines with the surface originating from the band, which becomes occupied for a short interval between the M and Γ points [Fig. 4(d)]. This combination produces the complicated Fermi surface around the M-A axis. Additionally, Fig. 4(b) contains a very small electron pocket centered on a point along the X-R line. The Fermi surface for $x = 3$ (not shown) is highly complex, since a

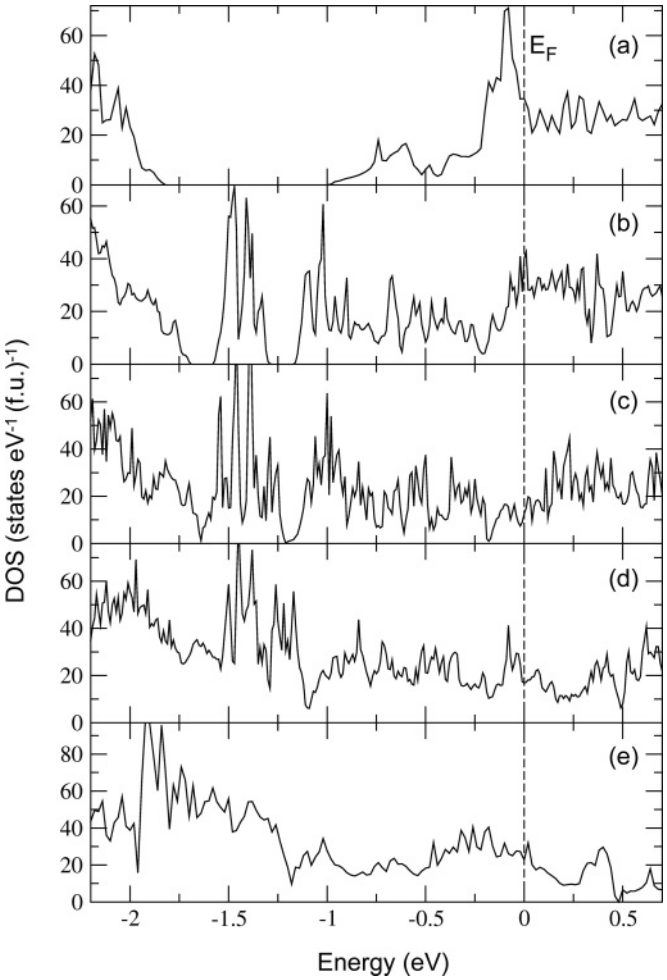

FIG. 6. Energy dependence of the total density of states near the Fermi level of $Ba_8Ni_xSi_{46-x}$ for $x = 0$ (a), 2 (b), 3 (c), 4 (d), and 6 (e). The vertical dashed line at 0 eV stands for the Fermi level.

total of eight bands cross the Fermi level. The highest five bands give rise to electron-like Fermi surfaces around the H point only [see Fig. 4(c)]. However, the band No. 2, for instance, contains both electron- and hole-like Fermi surfaces. These results clearly show that both holes and electrons contribute to the transport properties in these Ni-substituted clathrates. Furthermore, since this feature is inherent to the binary Ba_8Si_{46}, such multiband conduction might be a general characteristic shared by several $Ba_8M_xSi_{46-x}$ systems at least for low M contents.

The projection of the dispersion curves onto the energy axis results in the energy dependence of the total density of states (DOS) shown in Fig. 6. All compounds are metallic in nature. The electronic structure of Ba_8Si_{46} [Fig. 6(a)] is in good agreement with those reported previously in the literature.[38–40] A gap between −1.8 and −1.0 eV and a sharp peak located just below the Fermi level arising from the strong hybridization of the Ba 5d and Si 3p orbitals stand for the two main characteristics of the DOS. The gap is a feature inherited from the (hypothetical) empty Si_{46} clathrate in which all Si atoms have four Si neighbors as in α-Si. Filling the cages with Ba atoms introduces 16 extra electrons that should occupy the lower parts of the Si_{46} conduction band made up by antibonding Si 3p states. However, the hybridization of the Ba 5d orbitals that become occupied, with the Si 3p orbitals, makes the situation more complex than this simple picture. Nevertheless, the original gap of the Si_{46} clathrate is preserved, the DOS integrated between −1 eV, and the Fermi level giving exactly 16 electrons. The contribution of the Ba 5d orbitals to the DOS starts to be important mainly above −1 eV and their occupancies are 0.86 and 0.66 electrons for Ba in the small and large cages, respectively.

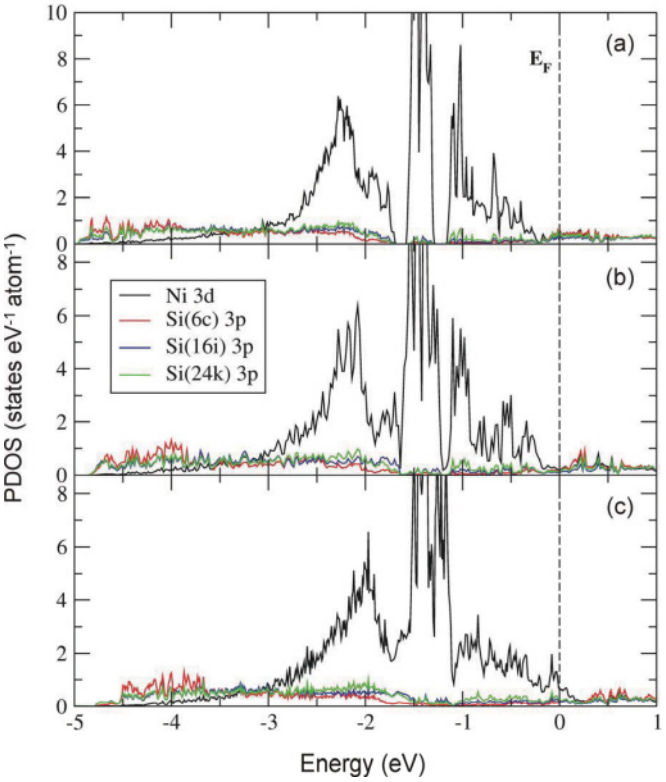

FIG. 7. (Color online) Partial density of states of $Ba_8Ni_xSi_{46-x}$ for $x = 2$ (a), 3 (b), and 4 (c). The vertical dashed line stands for the Fermi level.

The valence bands extend down to −12.6 eV. The region between −12.6 eV and −7.7 eV is dominated by Si 3s states. A group of Si 3s-3p bands of width ∼2 eV follows a pseudogap of ∼0.2 eV. A gap of ∼0.5 eV separates this group from a predominantly Si 3p band (with small admixtures of Ba 5d) covering the energy range −5 eV, −1.8 eV.

The substitution of Si by Ni atoms at the 6c position mainly results in three effects: (i) the valence electron count increases by 6 (including 3d electrons) for each Si → Ni exchange, (ii) nine orbitals of Ni (4s, 4p, 3d) replace four orbitals of Si, (iii) due to the larger atomic number of Ni, the bandwidth of the valence band region decreases with increasing Ni content (12.6 eV versus 11.5 eV for 0 and 6 Ni atoms in the formula unit, respectively) which is associated with a Ni-3d − Si-3p energy difference (charge transfer energy). Because of the second and third effects, a simple rigid band approach breaks down as already suggested by the variations in the dispersion curves. Among the Ni orbitals, the 3d's are the most relevant, and behave very differently in comparison to Si 3p orbitals. On one hand, the Ni 3d orbitals hybridize mainly with the Si 3p orbitals and on the other hand, they display atomic-like behavior giving rise to sharp features in the DOS. In addition, Ni 3d states have a narrower bandwidth and lie roughly between −5 and 2 eV. The Ni 3d occupation, as calculated from projected DOS, is 8.8 electrons and remains constant with x. Likewise, the Ba 5d occupations are also fairly constant and only slightly vary between 0.76 and 0.86 and between 0.62 and 0.66 electrons for Ba in small and large cages, respectively. The Ni-content dependence of the total DOS at the Fermi energy, $N(E_F)$, and its atom-resolved components are listed in Table III. $N(E_F)$ is mainly dominated by Si 3p states, the Ni contribution exceeding that of Ba only at $x = 4.0$. It is observed that $N(E_F)$ drops significantly from ∼35 to ∼10 states eV^{-1} $(f.u.)^{-1}$ when the Ni content is increased from $x = 2$ to $x = 3$. $N(E_F)$ starts to increase for $x > 3.0$ reaching ∼17 and ∼23 states eV^{-1} $(f.u.)^{-1}$ for $x = 4$ and 6, respectively. The large values of $N(E_F)$ at $x = 0$ and $x = 2.0$ in combination of a pseudogap opening at 0.25 and 0.5 eV most probably signal instability toward superconductivity, whereas the somewhat smaller values at $x = 4.0$ and 6.0 may hint at structural instability. Indeed, the latter does not form and the former is found to contain vacancies as mentioned above. The decrease of $N(E_F)$ with increasing concentration x of the substituting element was observed in other Si-based ternary type-I clathrates[30–32] and was correlated to the decrease of the superconducting transition temperature T_c with x.

The partial DOS depicting Ni 3d and Si 3p contributions for $x = 2$, 3, 4 are shown in Fig. 7. The contributions are referred to the Wyckoff positions in the original cell's space group after evaluating per atom averages in respective supercells. For $x = 2$, the sharp peaks around −1.5 eV originate from Ni 3d states. These states have negligible dispersion with a bandwidth of ∼0.3 eV. They are located inside the gap (between −1.70 and −1.15 eV) which is narrower by 0.25 eV than the gap observed in the binary Ba_8Si_{46} clathrate and are due to the Ni 3d orbitals exhibiting a more atomic-like behavior.[38–40]

TABLE IV. Values of the γ and β parameters along with the Debye temperature, θ_D, the theoretical values of the Sommerfeld coefficient, γ_{FPLO}, and the electron-phonon coupling constant $\lambda_{e-ph} = \gamma/\gamma_{\mathrm{FPLO}} - 1$.

Actual Ni content x	γ (mJ mol^{-1} K^{-2})	β (mJ mol^{-1} K^{-4})	θ_D (K)	γ_{FPLO} (mJ mol^{-1} K^{-2})	λ_{e-ph}
2.6	56.1	1.15	450	47.6	0.18
2.7	51.7	1.08	460	41.6	0.24
2.8	47.2	0.98	474	35.2	0.34
2.9	32.0	1.16	448	29.2	0.10
3.1	26.8	1.38	424	24.1	0.11
3.4	30.8	1.32	430	29.0	0.06
3.8	27.9	1.31	431	35.6	/

These weakly dispersing Ni 3*d* states are observable also for $x = 3$ around -1.5 eV with a larger bandwidth of $\sim$0.45 eV. The original gap disappears and two pseudogap-like features develop at -1.65 and -1.20 eV. With a further increase of the Ni content (i.e., $x = 4$), no sign of the original gap is observed. Although Ni 3*d* states still display sharp features in the DOS, the corresponding bands (not shown) are actually more dispersive. These modifications in the electronic structure generated by the Ni substitution are qualitatively similar to those observed in the $Ba_8Ga_xSi_{46-x}$, $Ba_8Cu_xSi_{46-x}$, and $Ba_8Ag_xSi_{46-x}$ systems.[30–32]

To summarize this part, as the Ni content increases, so does the number of weakly dispersing Ni *3d* states. Thus, these states start filling the band gap originating from the hypothetical Si_{46} clathrate. Furthermore, these states show increasing hybridization (both Ni-Si and Ni-Ni) with increasing x, so that a transition from the isolated *d* bands ($x = 2$) to the appearance of pseudogaps ($x = 3$), and finally to a gapless band structure ($x = 4$) occurs.

C. Specific heat

Figure 8(a) shows C_p/T as a function of T^2 in the temperature range 1.9–15 K for the illustrative $x = 3.1$ clathrate. Although the parent compound Ba_8Si_{46} becomes superconducting below $\sim$8 K,[41,42] no superconducting transition could be observed down to 1.9 K in the Ni-substituted samples for $2.4 \leqslant x \leqslant 3.8$. This result is consistent with previous studies revealing that substituting either on the Ba or on the Si site tends to decrease the critical temperature, T_C.[42] Several theoretical studies have indicated that superconductivity is an intrinsic property of the sp^3 network, therefore suggesting that the similarity between Ga or Ge atoms and Si helps maintain superconductivity.[30–32,41] This hypothesis seems to be further corroborated by results obtained in the $Ba_8Cu_xSi_{46-x}$ system for which T_C was drastically lowered down to 2.9 K for $x = 4.0$.[31] To clarify whether superconductivity survives the addition of Ni and thus, appears at lower temperatures, further measurements down to 0.4 K using the He_3 option of a PPMS were carried out. No superconducting transition could be detected above 0.4 K demonstrating that replacing $\sim$6 at% of Si atoms prevents the formation of a superconducting state. Magnetic susceptibility data (see below) have clearly shown that Ni atoms are in a nonmagnetic state ruling out the magnetic pair-breaking effect (i.e., interaction of magnetic moments with conduction electrons breaking the time-reversal symmetry of the Cooper pairs and leading to a strong reduction of T_C with x). Thus, the observed variation seems to support the idea of a direct link between the strong decrease of T_C and $N(E_F)$ via the electron-phonon coupling constant, λ_{e-ph}, at least above $x = 2.0$. Between $x = 0$ and $x = 2.0$, however, our electronic band structure calculations suggest a negligible influence of Ni on $N(E_F)$ which might preserve the existence of a superconducting state. Clearly, further experiments at lower Ni contents are required to pin down the exact variations in T_C across the entire possible Ni concentration range.[34] To further explore whether the variations in $N(E_F)$ trace the disappearance of T_C for $0 \leqslant x \leqslant 3.8$, the Sommerfeld coefficient, γ, which reflects the renormalized density of states $(1 + \lambda_{e-ph})N(E_F)$, was extracted from the low-temperature regions (1.8–6 K) using the conventional relation $C_p/T = \gamma + \beta T^2$ where βT^2 is the lattice contribution. The inferred γ and β values are listed in Table IV.

Within the Debye model, the β coefficient is related to the Debye temperature through $\theta_D = (12\pi^4 nR/5\beta)^{1/3}$ where n is the number of atoms per formula unit and R is the gas constant. With $n = 54$ for all samples, we obtain θ_D in the range $\sim$420–470 K regardless of the Ni content. These values are slightly higher but coherent with that reported for Ba_8Si_{46} ($\theta_D \sim 370$ K) and suggest that the phonon spectrum is not significantly modified in the presence of Ni atoms.[43]

As suggested by our band structure calculations, the $x = 3.0$ composition delineates two regions. Below this value, γ strongly decreases with the Ni content before increasing up to $x = 3.8$ [Fig. 8(b)]. Assuming a linear variation in $N(E_F)$ with different slopes between $x = 2.0$ and 3.0 and $x = 3.0$ and 4.0, an estimation of λ_{e-ph} can be inferred (Table IV). The presence of Ni drastically depresses the λ_{e-ph} values from 0.8 to 1.2 in Ba_8Si_{46} down to 0.1 at $x = 2.9$ reflecting the decrease in $N(E_F)$.[43,44] At higher Ni contents, however, the theoretical γ values overestimate the experimental ones. Our detailed structural and chemical characterizations have shown that vacancies are present in the crystal structure at high Ni contents and may be a reason for the observed discrepancy. Further calculations taking into account vacancies may help to determine their influence on the electronic band structure of these compounds. Several studies undertaken on the Ba_8Si_{46} compound and on its ternary derivatives have shown that the thermodynamic properties of the superconducting state can be satisfactorily described within the BCS theory.[42,43] Assuming that this result can be extended to these Ni substituted

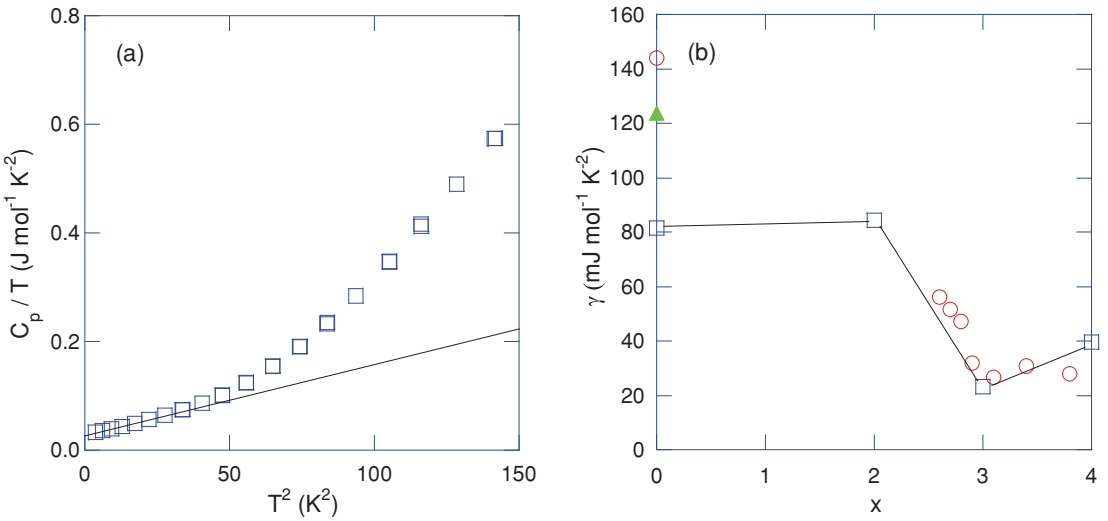

FIG. 8. (Color online) (a) C_p/T as a function of T^2 for the illustrative $x = 3.1$ sample. Note that all the samples studied display a similar temperature dependence. The solid line is a guide to the eye to underline the narrow temperature window where a linear dependence is observed. (b) Sommerfeld coefficient, γ, as a function of the Ni content. The open red circle symbols refer to the experimental γ values whereas the open blue squares stand for the theoretical values inferred from band structure calculations. The solid green up-triangle symbol refers to the experimental value of Ba_8Si_{46} obtained from specific heat measurements in Ref. 44.

compounds, the superconducting transition temperature can be estimated using the λ_{e-ph} values and the McMillan formula[45]:

$$T_C = \frac{\theta_D}{1.45} \exp\left(\frac{-1.04(1+\lambda_{e-ph})}{\lambda_{e-ph} - \mu^*(1+0.62\lambda_{e-ph})}\right), \qquad (1)$$

where μ^* is the effective electron-electron repulsion. The value of this parameter was estimated to be ~0.23 for Ba_8Si_{46} from measurements of the superconducting isotope coefficient.[43] Though this value is higher than those usually assumed in conventional superconductors (~0.1–0.15) and thus at the border of the BCS theory, it appears to be consistent with the theoretical value ~0.24.[46] Assuming that μ^* does not appreciably vary across the Ni concentration range and taking the θ_D values derived from the lattice contribution to the specific heat, the values of λ_{e-ph} obtained are clearly too low to induce a superconducting transition in these samples. In addition, a maximum T_C of 0.4 K in Eq. (1) alternatively gives a lower limit of $\mu^* = 0.21$, further supporting a large value of this parameter in Ba_8Si_{46} and its ternary derivatives. This result might hint toward a more complex mechanism involved in the formation of the superconducting condensate such as two-gap superconductivity as recently suggested by tunneling-spectroscopy experiments carried out on Ba_8Si_{46}.[47] In addition, these results complement previous reports indicating that the variations in $N(E_F)$ primarily govern the superconducting transition temperature in Si-based type-I clathrates.[40,42]

D. Magnetic susceptibility

The temperature dependence of the magnetic susceptibility, χ, of $Ba_8Ni_xSi_{46-x}$ is shown in Fig. 9. It is worth mentioning that measurements of the isothermal magnetization curves, $M(H)$, performed at 5 and 300 K revealed a perfect linearity up to 5 T and thus, the absence of ferromagnetic impurities. Regardless of the Ni content, χ is negative and quasi-temperature-independent down to ~20 K indicative of diamagnetic behavior. These results indicate that Ni assumes $3d^{10}$ electronic configuration and thus possesses a zero-spin state in these compounds. This conclusion is further confirmed by investigations of the local structure surrounding the Ni atoms via x-ray absorption near edge structure (XANES) measurements described in detail elsewhere.[34] Traces of Curie-paramagnetic impurities are likely responsible for the upturns toward low temperatures that result in positive values at 2 K in the $x = 3.1$ and 3.4 samples. At room temperature, the magnetic susceptibility reaches values ranging between -600 and -1200×10^{-6} emu mol^{-1}. These values are consistent with that of the parent Ba_8Si_{46} compound estimated to be -1150×10^{-6} emu mol^{-1}.[43] An estimation of the core diamagnetic values, χ_{dia}, can be obtained by subtracting the Pauli susceptibility contribution, χ_{Pauli}, which arises from the contribution of magnetically nonpolarized charge carriers. The Pauli susceptibility is related to $N(E_F)$ via $\chi_{Pauli} = 2.376 \times 10^{-6} \times N(E_F)$ where χ_{Pauli} and $N(E_F)$ are expressed in emu mol^{-1} and states Ry^{-1}, respectively. Using the calculated $N(E_F)$ values (Table III), the χ_{Pauli} values can be inferred and are summarized in Table V. Note that, as a first approximation, the theoretical $N(E_F)$ values for $x = 2.6$, 2.8, 2.9, and 3.4 were estimated assuming a linear variation of $N(E_F)$ with two different slopes for x varying between 2.0 and 3.0 and between 3.0 and 4.0, respectively. Within this assumption, the core diamagnetic contributions obtained are roughly similar across the entire Ni concentration range (Table V). Even though none of the samples studied contain any paramagnetic phases, additional diamagnetic contributions originating from secondary phases may also play a role in the observed differences. In addition, these values can be compared to the expected χ_{dia} values estimated using the tabulated diamagnetic contributions of closed-shell cations (Table V).[48] This yields (absolute) values significantly lower than the experimental ones pointing to the presence of an extra source of diamagnetism in these

TABLE V. Values of the diamagnetic contributions estimated from tabulated closed-shell cation contributions χ_{dia}^{theo}, the Pauli susceptibilities inferred from electronic band structure calculations (χ_{Pauli}^{FPLO}), and the experimental diamagnetic contributions at 300 K $\chi_{dia} = \chi - \chi_{Pauli}^{FPLO}$. All these values are expressed in 10^{-6} emu mol^{-1}.

Actual Ni content x	χ_{dia}^{theo}	χ_{Pauli}^{FPLO}	χ_{dia}
2.6	−330.6	653.7	−1268.5
2.8	−332.8	483.4	−1141.9
2.9	−333.9	401.0	−1551.0
3.1	−336.1	313.1	−1419.1
3.4	−340.5	431.4	−1351.4
3.8	−343.8	543.2	−1376.2

compounds, which cannot be attributed to the small amount of secondary phases. This discrepancy is, however, restricted neither to $Ba_8Ni_xSi_{46-x}$ nor to clathrate structures and several other intermetallic compounds such as $CoSb_3$ or $RuAl_2$ are known to exhibit enhanced diamagnetism.[49,50] Though the exact underlying mechanism in these materials remains an unsettled issue, it was suggested that molecular-ring currents, induced by the Lorentz force under an applied magnetic field and responsible for the magnetic properties of carbon allotropes and aromatic molecules, might be equally at play in clathrates.[51,52] However, this mechanism is not firmly established in clathrates and clearly requires further theoretical and experimental studies before drawing any final conclusion.

E. Galvanomagnetic and thermoelectric properties

The temperature dependence of the electrical resistivity of $Ba_8Ni_xSi_{46-x}$ is shown in Fig. 10. All the samples studied display a positive electrical resistivity coefficient $d\rho/dT$ indicative of metallic behavior in agreement with our band structure calculations. For $x = 2.6$, 2.8, 2.9, 3.4, and 3.8, the electrical resistivity exhibits a metallic-like behavior down to

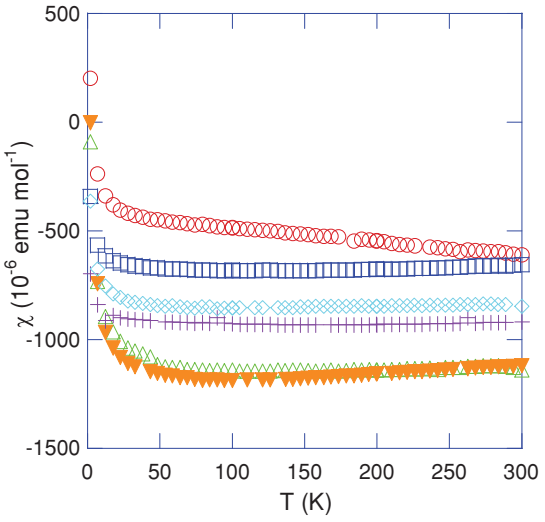

FIG. 9. (Color online) Temperature dependence of the magnetic susceptibility of $Ba_8Ni_xSi_{46-x}$ for $x = 2.6$ (open red circle), 2.8 (open blue square), 2.9 (open green up-triangle), 3.1 (solid orange down-triangle), 3.4 (blue cross), and 3.8 (open turquoise diamond).

TABLE VI. Values of the Debye temperature, θ_D, the coefficient of the phonon contribution to the electrical resistivity, R, and the residual electrical resistivity, ρ_0, as determined from the best fits to the data according to the Bloch-Grüneisen law [Eq. (2)]. Note that the ρ_0 values are expressed here in $\mu\Omega$ cm.

Actual Ni content x	θ_D (K)	R ($\mu\Omega$cmK^{-1})	ρ_0($\mu\Omega$cm)
2.6	343	7.8	244
2.8	243	5.8	218
2.9	206	5.3	270
3.1	578	8.7	297
3.4	404	16.6	355
3.8	287	13.9	288

∼30 K and then slightly levels off at lower temperatures. The electrical resistivity of the $x = 3.1$ sample assumes quasi-constant values below 50 K to become weakly temperature dependent above this temperature up to 350 K. The $d\rho/dT$ coefficient varies across the Ni concentration range. The temperature dependence of ρ in simple metals and metallic alloys is usually dominated by electron-phonon scattering and is quantitatively expressed through the Bloch-Grüneisen law,[53]

$$\rho(T) = \rho_0 + 4\theta_D R \left(\frac{T}{\theta_D}\right)^5 \int_0^{\theta_D/T} \frac{x^5 dx}{(e^x - 1)(1 - e^{-x})}, \quad (2)$$

where ρ_0 is the temperature-independent residual resistivity and R is the coefficient of the phonon contribution to the electrical resistivity which mainly controls the $d\rho/dT$ values. The variations in the R values should therefore reflect the variations in the electron-phonon coupling strength. The observed variation in R, inferred from least-squares fits to the data according to Eq. (2) using ρ_0, R, and θ_D as free parameters, seems to be in agreement with this picture (Table VI). However, even though a discrepancy between the Debye temperatures obtained from the Bloch-Grüneisen law and those extracted from specific heat analyses is usually observed due to the fact that only the longitudinal phonons are taken into account in deriving Eq. (2), marked differences appear in the present case. In the absence of electronic and magnetic correlations, such discrepancy may be a sign of a multiband conduction as suggested by our band structure calculations.

In the whole temperature range, the ρ values are only slightly sensitive to the Ni content and range between 2.8 $\mu\Omega.m$ and 4.6 $\mu\Omega.m$ at room temperature (Table VII). No clear trend toward lower or higher ρ values with Ni substitution can be observed in these data. The theoretical prediction that both holes and electrons are involved in the electrical conduction of these materials may explain this behavior, since the mobilities along with the hole and electron concentrations are intimately related to the Ni content and to the subtleties of the band structure, specifically near the $x = 3.0$ composition. However, slight differences in the microstructure and in the amount of secondary phases that vary across this series of samples may potentially mask any real x dependence in the data.

TABLE VII. Room temperature values of the electron concentration (n), Seebeck coefficient (α), and electrical resistivity (ρ) of the different $Ba_8Ni_xSi_{46-x}$ compounds studied. The total thermal conductivity (λ) values are given at 200 K due to the radiative contribution responsible for the slight upturns above this temperature.

Actual Ni content x	n (10^{21} cm^{-3})	α (μV K^{-1})	ρ ($\mu\Omega$ m)	λ (W m^{-1} K^{-1})
2.6	7.0	−13.3	3.0	4.4
2.8	5.2	−11.1	2.8	4.6
2.9	3.5	−11.4	3.3	4.6
3.1	3.5	−7.0	3.3	4.3
3.4	4.1	−17.6	4.5	4.0
3.8	4.5	−26.1	4.0	4.2

Hall effect experiments, performed in the 10- to 300-K temperature range, provide additional information regarding the effect of the Ni content on the electronic band structure. Figure 11(a) shows the Hall resistivity, ρ_{xy}, as a function of the magnetic field at selected temperatures for the illustrative $x = 3.4$ clathrate. To exclude the longitudinal magnetoresistive contribution coming from misalignment of contacts, the Hall resistivity was derived from the antisymmetric part of the transverse resistivity under magnetic field reversal following the formula $(\rho_{xy}(+\mu_0 H) - \rho_{xy}(-\mu_0 H))/2$. For all samples, $\rho_{xy}(\mu_0 H)$ data are linear with a negative slope in the whole temperature and field ranges investigated indicative of a dominant electron-like signal. No indications of departure from linearity as may be expected from the presence of both types of carrier can be observed in the present data. Assuming that both carriers contribute to the measured Hall signal, this absence of departure may then indicate that holes remain in the low-field limit ($\mu_p B \ll 1$ where μ_p is the hole mobility) in the field range covered by our experiments. The Hall coefficient, R_H, inferred from the slope of the $\rho_{xy}(\mu_0 H)$ curves, is weakly temperature dependent for the $x = 2.6$ and 3.4 samples and is consistent with the metallic nature of these compounds [Fig. 11(b)]. The temperature dependence of the $x = 2.9$ sample is somewhat stronger, with the $|R_H|$ values decreasing with increasing temperature from 2.85×10^{-3} at 10 K to 1.90×10^{-3} cm^3 C^{-1} at 275 K. Within a single-band picture, this would correspond to an increase of the electron concentration, n, from 2.15×10^{21} at 10 K up to 3.3×10^{21} cm^{-3} at 275 K using the single-carrier relation $R_H = -r_H/en = -1/en$ whereby the Hall factor, r_H, is assumed to be equal to 1. The dependence of r_H on the scattering mechanisms of the charge carriers and thus, on temperature, usually results in a slight increase of R_H with temperature regardless of the degeneracy of the system. Given the similar compositions of the samples studied, significant differences in the scattering mechanisms seem unlikely. The temperature dependence of the $x = 2.9$ sample might therefore be a hint indicating that both holes and electrons contribute to the Hall signal. Nevertheless, adopting a single-band model to derive n at room temperature (Table VII) leads to a decrease of n with increasing x up to $x = 3.1$ before slightly increasing up to $x = 3.8$. In any case, the variations in n as a function of the Ni content are consistent with an overall decrease in $N(E_F)$ as previously discussed.

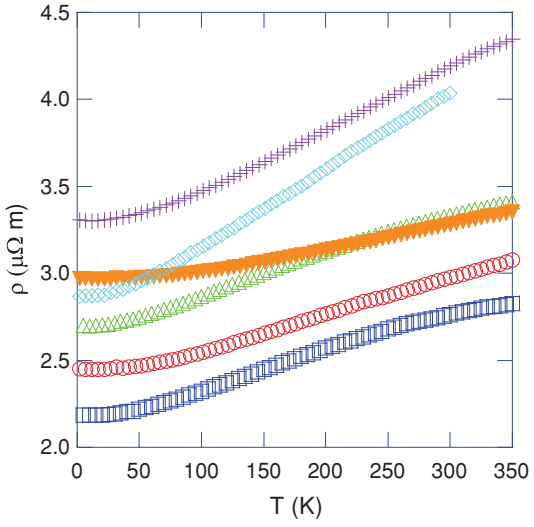

FIG. 10. (Color online) Temperature dependence of the electrical resistivity of $Ba_8Ni_xSi_{46-x}$ for $x = 2.6$ (open red circle), 2.8 (open blue square), 2.9 (open green up-triangle), 3.1 (solid orange down-triangle), 3.4 (purple cross), and 3.8 (open blue diamond).

Though direct experimental evidence of the contribution of both types of carriers remain elusive from electrical resistivity and Hall effect data, the temperature and x dependencies of the thermopower, shown in Fig. 12, yield clues that uncover their presence. Regardless of the Ni content, α increases in absolute value with increasing temperature to reach values ranging between −7 and −26 μV K^{-1} at 300 K (Table VII). The negative sign of α suggests that electrons dominate the electrical conduction and is therefore consistent with a dominant electron-like response in the Hall effect measurements. Thus, while the $Ba_8Au_xSi_{46-x}$ and $Ba_8Au_xGe_{46-x-y}\square_y$ systems both exhibit n type-p type transitions, the $Ba_8Ni_xSi_{46-x}$ and $Ba_8Ni_xGe_{46-x-y}\square_y$ compounds do not share this property.[19–21] These results also reveal a nonmonotonic behavior of the thermopower with x. At low Ni contents, $\alpha(T)$ varies linearly before evolving into a nonlinear dependence upon decreasing temperature, the departure from linearity being stronger as the Ni content is slightly increased from $x = 2.8$ to $x = 2.9$. Such behavior is not confined to these compounds and qualitatively resembles those of the $Ba_8Pt_xSi_{46-x}$ and $Ba_8Pd_xSi_{46-x}$ systems in which complex variations in $\alpha(T)$ as a function of temperature and substitution level were observed.[28] A transition from negative to positive values occurs below 20 K in the $x = 2.9$ sample with a maximum of ∼8 μV K^{-1} at 10 K. A maximum in α at low temperatures is usually related to a phonon or magnon-drag effect. However, the diamagnetic

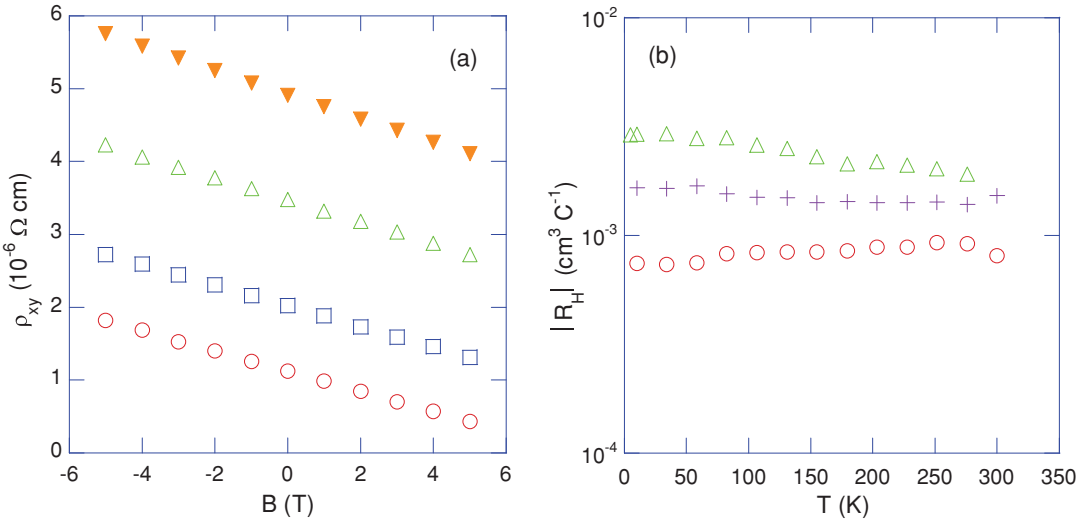

FIG. 11. (Color online) (a) Field dependence of the Hall resistivity, ρ_{xy}, of the illustrative $x = 3.4$ sample at 275 K (open red circle), 200 K (open blue square), 130 K (open green up-triangle), and 10 K (slide orange down-triangle). (b) Temperature dependence of the Hall coefficient, $|R_H|$, of $Ba_8Ni_xSi_{46-x}$ for $x = 2.6$ (open orange circle), 2.9 (open green up-triangle), and 3.4 (blue cross).

nature of the samples studied and the lack of coincidence of the peak temperature and the temperature of the dielectric maximum in the thermal conductivity (see below) suggest a different origin. The observed positive values of α together with the negative slope of the $\rho_{xy}(\mu_0 H)$ curves clearly show that both holes and electrons are involved in the electrical conduction processes. Another conclusive signature is related to the variations in α with x. As evidenced in Table VII, at room temperature, α first decreases with increasing x before increasing with further addition of Ni. The concomitant drop in α and in the carrier concentration as shown by Hall effect data is unusual and contrasts with the expectation of an increase of the diffusion part of the thermopower, α_d, with decreasing carrier concentration following the free-electron relation,[54]

$$\alpha_d = \frac{\pi^2 k_B^2 2m_e}{e\hbar^2(3n\pi^2)^{2/3}}T, \tag{3}$$

where k_B is the Boltzmann constant, m_e is the electron mass, e is the elementary charge, and $\hbar$ is the Planck constant. Note that this relation is valid above θ_D where the electron-phonon scattering is expected to be the dominant scattering mechanism. In the present case, thermopower measurements performed at high temperatures have shown that the slope is temperature independent, enabling one to apply this relation at temperatures slightly below θ_D. Attempting to fit the $\alpha(T)$ data in the 250- to 350-K temperature range using Eq. (3) then yields an estimation of the charge carrier concentration, n, which amounts to 9.6×10^{21}, 2.1×10^{22}, 2.6×10^{22}, 1.3×10^{22}, 5.1×10^{21}, and 3.8×10^{21} cm^{-3} for $x = 2.6$, 2.8, 2.9, 3.1, 3.4, and 3.8, respectively. At low Ni contents ($x < 3.4$), these values significantly differ from those derived from Hall effect data. At higher Ni concentrations ($x = 3.4$ and 3.8), however, a fairly good agreement is achieved and shows that the thermal diffusion of charge carriers then dominates the temperature dependence of α. A possible explanation of this discrepancy could be related to the effective mass of the charge carriers significantly differing from the bare electron mass. In the present case, the above-mentioned values would imply an effective mass ranging between 0.15 and 0.35 for $x = 2.8$, 2.9, and 3.1. Even though variations in the effective mass with x cannot be strictly ruled out, the inapplicability of Eq. (3) at low substitution levels may rather reflect a hole contribution to the thermopower of increasing importance as the Ni content is approaching $x = 3.0$ where a quasicompensation seems to be achieved. The smaller magnitude of α as the carrier concentration decreases may therefore originate from x-dependent hole and electron contributions to the thermopower which, in a two-band system, is expressed as

$$\alpha = (\sigma_p S_p + \sigma_n S_n)/(\sigma_p + \sigma_n), \tag{4}$$

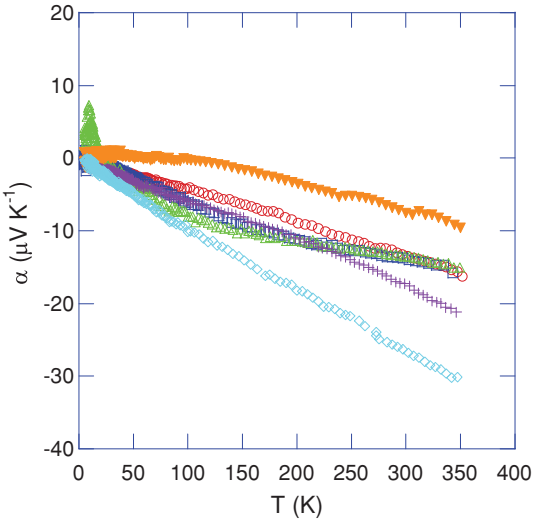

FIG. 12. (Color online) Temperature dependence of the thermopower of $Ba_8Ni_xSi_{46-x}$ for $x = 2.6$ (open red circle), 2.8 (open blue square), 2.9 (open green up-triangle), 3.1 (solid orange down-triangle), 3.4 (blue cross), and 3.8 (open turquoise diamond).

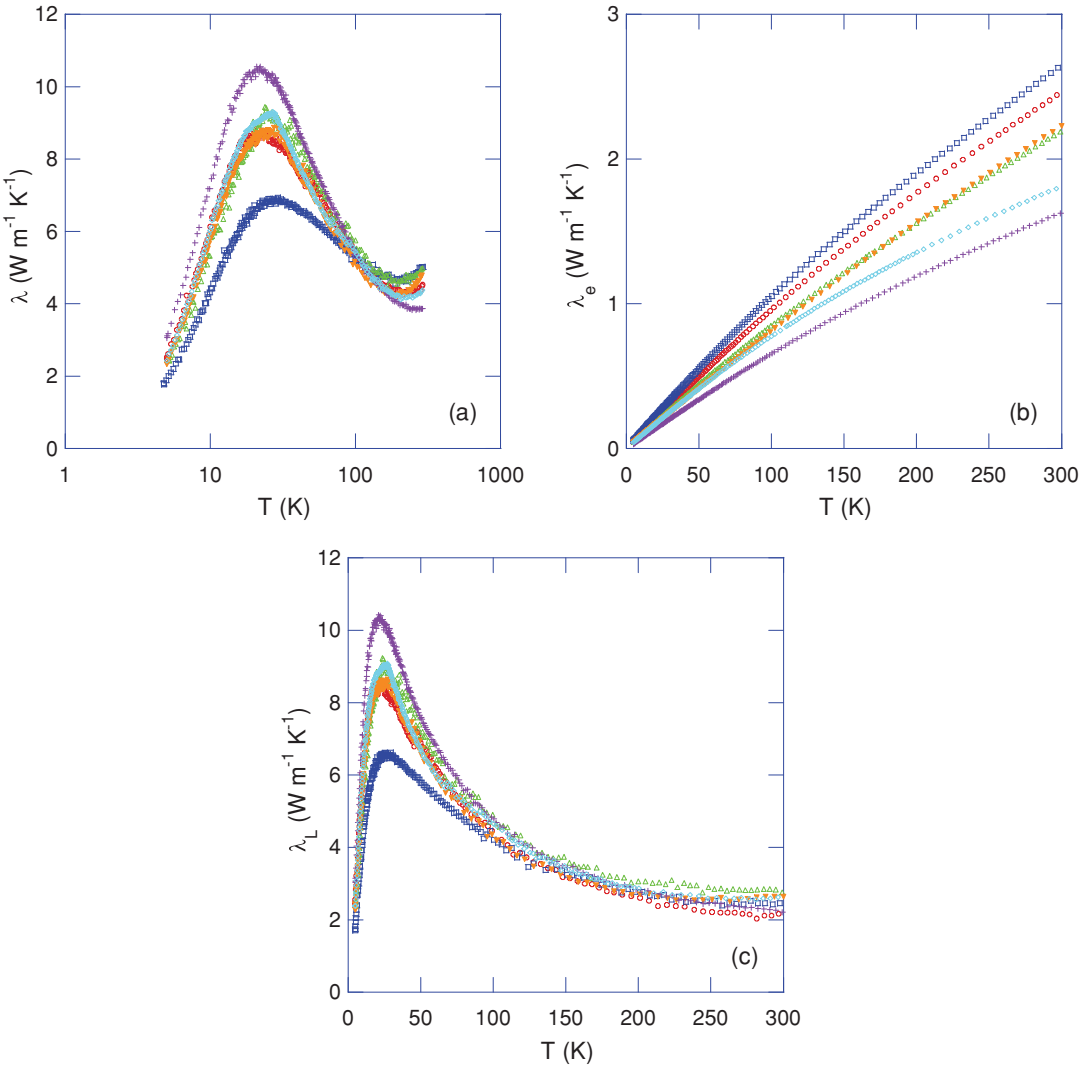

FIG. 13. (Color online) Temperature dependence of the total (a), electronic (b), and lattice (c) thermal conductivity of $Ba_8Ni_xSi_{46-x}$ for $x = 2.6$ (open red circle), 2.8 (open blue square), 2.9 (open green up-triangle), 3.1 (solid orange down-triangle), 3.4 (blue cross), and 3.8 (open turquoise diamond).

where S_p and S_n stand for the thermopower contributions of holes and electrons, respectively, whereas σ_p and σ_n are the respective partial electrical conductivities of holes and electrons.

The temperature dependence of the total thermal conductivity is shown in Fig. 13(a). All the samples exhibit similar temperature dependence typical of simple crystalline insulators: the low-temperature region is dominated by a pronounced dielectric maximum followed by an approximately T^{-1} dependence associated with propagating phonons scattered by anharmonic interactions. As expected from such close compositions, the thermal conductivity values remain quasiconstant as the Ni concentration spans the range $2.6 \leqslant x \leqslant 3.8$. The observed difference in magnitude of the dielectric maximum values near 25 K may be due to slight differences in the microstructure and to the varying amount of secondary phases present in our collection of samples. Nevertheless, the quasi-independence of the thermal conductivity with respect to x is consistent with the specific heat data suggesting minimal impact of an increase in the Ni content on the thermal properties of these materials. The experimental values of the thermal conductivity and of the electrical resistivity allow the lattice thermal conductivity, λ_L, to be extracted by subtracting the electronic contribution, which can be estimated using the Wiedemann-Franz law $\lambda_e = LT/\rho$ where L is the Lorenz number [Figs. 13(b) and 13(c)]. As a first approximation, L was assumed to be equal to the value of the degenerate electron gas $L = L_0 = 2.44 \times 10^{-8}\,V^2\,K^{-2}$. All the samples exhibit similar low λ_L values in agreement with those observed in various Ge-, Sn-, and Si-based type-I clathrates.[1] As expected from the metallic nature of these samples, the dimensionless figure of merit ZT are very low (0.02 at 300 K for $x = 3.8$) requiring further tuning of the charge carrier concentration.

IV. SUMMARY

Thermoelectric, galvanomagnetic, and magnetic properties measurements were performed on polycrystalline type-I clathrate $Ba_8Ni_xSi_{46-x}$. First-principles calculations have revealed a nonrigid behavior of the electronic band structure

and strong variations in $N(E_F)$ with x. These theoretical results are in line with experimental findings *viz*., the variations in the electronic properties with the Ni content (i.e., a strongly depressed electron-phonon coupling strength) as well as nonmonotonic variations in electrical resistivity and thermopower as x increases. In addition, the thermopower data appear consistent with a picture suggested by Fermi surface calculations, whereby both holes and electrons are involved in the electrical conduction in these materials. Magnetic susceptibility data indicate that the Ni atoms have a nonmagnetic state in these clathrates. All these results highlight the sensitivity of the electronic properties to the Ni content suggesting that these properties may not be confined to the Ni substitution but may be observed in other ternary Si-based type-I clathrates. The metallic nature of $Ba_8Ni_xSi_{46-x}$ prevents achieving high ZT values in the temperature range investigated. Further adjustment of the carrier concentration through another partial substitution such as Ga or Au may be worthwhile to consider and will help further assess the thermoelectric potential of Si-based type-I clathrates.

ACKNOWLEDGMENTS

The authors warmly thank Petra Scheppan, Renate Hempel-Weber, and members of the Kompetenzgruppe Struktur for providing experimental support. C.C. acknowledges the financial support of the CNRS-MPG program.

*candolfi@cpfs.mpg.de
†ormeci@cpfs.mpg.de

[1] M. Christensen, S. Johnsen, and B. B. Iversen, Dalton Trans. **39**, 978 (2010).
[2] G. S. Nolas, G. A. Slack, and S. B. Schujman in *Semiconductors and Semimetals*, edited by T. M. Tritt, Vol. 69 (Academic Press, Burlington, 2001), p. 255.
[3] A. San Miguel, Chem. Soc. Rev. **35**, 876 (2006).
[4] H. J. Goldsmid, in *Thermoelectric Refrigeration* (Temple Press Books, London, 1964).
[5] E. S. Toberer, M. Christensen, B. B. Iversen, and G. J. Snyder, Phys. Rev. B **77**, 075203 (2008).
[6] X. Shi, J. Yang, S. Bai, J. Yang, H. Wang, M. Chi, J. R. Salvador, W. Zhang, L. Chen, and W. Wong-Ng, Adv. Funct. Mater **20**, 755 (2010).
[7] K. A. Kovnir and A. V. Shevelkov, Russ. Chem. Rev. **73**, 923 (2004).
[8] E. Reny, S. Yamanaka, C. Cros, and M. Pouchard, Chem. Comm. **24**, 2505 (2000).
[9] N. Jaussaud, P. Toulemonde, M. Pouchard, A. San Miguel, P. Gravereau, S. Pechev, G. Goglio, and C. Cros, Solid State Sci. **6**, 401 (2004).
[10] U. Aydemir, C. Candolfi, H. Borrmann, M. Baitinger, A. Ormeci, W. Carrillo-Cabrera, C. Chubilleau, B. Lenoir, A. Dauscher, N. Oeschler, F. Steglich, and Yu. Grin, Dalton Trans. **39**, 1078 (2010).
[11] N. Melnychenko-Koblyuk, A. Grytsiv, St. Berger, H. Kaldarar, H. Michor, F. Röhrbacher, E. Royanian, E. Bauer, P. Rogl, H. Schmid, and G. Giester, J. Phys. Condens. Matter **19**, 046203 (2007).
[12] N. Melnychenko-Koblyuk, A. Grytsiv, L. Fornasari, H. Kaldarar, H. Michor, F. Röhrbacher, M. M. Koza, E. Royanian, E. Bauer, P. Rogl, M. Rotter, H. Schmid, F. Marabelli, A. Devishvili, M. Doerr, and G. Giester, J. Phys. Condens. Matter **19**, 216223 (2007).
[13] N. Melnychenko-Koblyuk, A. Grytsiv, P. Rogl, M. Rotter, E. Bauer, G. Durand, H. Kaldarar, R. Lackner, H. Michor, E. Royanian, M. M. Koza, and G. Giester, Phys. Rev. B **76**, 144118 (2007).
[14] N. Melnychenko-Koblyuk, A. Grytsiv, P. Rogl, M. Rotter, R. Lackner, E. Bauer, L. Fornasari, F. Marabelli, and G. Giester, Phys. Rev. B **76**, 195124 (2007).
[15] S. Johnsen, A. Bentien, G. K. H. Madsen, B. B. Iversen, and M. Nygren, Chem. Mater **18**, 4633 (2006); H. Zhang, H. Borrmann, N. Oeschler, C. Candolfi, W. Schnelle, M. Schmidt, U. Burkhardt, M. Baitinger, J.-T. Zhao, and Yu. Grin, Inorg. Chem. **50**, 1250 (2011).
[16] H. Anno, M. Hokazono, M. Kawamura, J. Nagao, and K. Matsubara, in *Proceedings of the 21st International Conference on Thermoelectrics* (IEEE, New York, 2002), pp. 77–80.
[17] A. Bentien, M. Christensen, J. D. Bryan, A. Sanchez, S. Paschen, F. Steglich, G. D. Stucky, and B. B. Iversen, Phys. Rev. B **69**, 045107 (2004).
[18] M. Christensen, F. Juranyi, and B. B. Iversen, Physica B **385/386**, 505 (2006).
[19] M. Christensen, N. Lock, J. Overgaard, and B. B. Iversen, J. Am. Chem. Soc. **128**, 15657 (2006).
[20] S. K. Deng, X. F. Tang, and Q. J. Zhang, J. Appl. Phys. **102**, 043702 (2007).
[21] H. Anno, M. Hokazono, H. Takakura, and K. Matsubara, in *Proceedings of the 24th International Conference on Thermoelectrics* (IEEE, New York, 2005), pp. 102–105.
[22] S. Johnsen, A. Bentien, G. K. H. Madsen, M. Nygren, and B. B. Iversen, Phys. Rev. B **76**, 245126 (2007).
[23] N. Jaussaud, P. Gravereau, S. Pechev, B. Chevalier, M. Ménétrier, P. Dordor, R. Decourt, G. Goglio, C. Cros, and M. Pouchard, C. R. Chimie **8**, 39 (2005).
[24] D. Shu-Kang, T. Xin-Feng, and T. Run-Sheng, Chin. Phys. B **18**, 3084 (2009).
[25] V. L. Kuznetsov, L. A. Kuznetsova, A. E. Kaliazin, and D. M. Rowe, J. Appl. Phys. **87**, 7871 (2000).
[26] D. Nataraj, J. Nagao, M. Ferhat, and T. Ebinuma, J. Appl. Phys. **93**, 2424 (2003).
[27] C. L. Condron, J. Martin, G. S. Nolas, P. M. B. Piccoli, A. J. Schultz, and S. M. Kauzlarich, Inorg. Chem. **45**, 9381 (2006).
[28] N. Melnychenko-Koblyuk, A. Grytsiv, P. Rogl, E. Bauer, R. Lackner, E. Royanian, M. Rotter, and G. Giester, J. Phys. Soc. Jpn. **77**, 54 (2008).
[29] N. Nasir, A. Grytsiv, N. Melnychenko-Koblyuk, P. Rogl, E. Bauer, R. Lackner, E. Royanian, G. Giester, and A. Saccone, J. Phys. Condens. Matter **21**, 385404 (2009).
[30] Y. Li, R. Zhang, Y. Liu, N. Chen, Z. P. Luo, X. Ma, G. Cao, Z. S. Feng, C.-R. Hu, and J. H. Ross, Phys. Rev. B **75**, 054513 (2007).
[31] Y. Li, Y. Liu, N. Chen, G. Cao, Z. Feng, and J. H. Ross, Phys. Lett. A **345**, 398 (2005).
[32] N. Kamakura, T. Nakano, Y. Ikemoto, M. Usuda, H. Fukuoka, S. Yamanaka, S. Shin, and K. Kobayashi, Phys. Rev. B **72**, 014511 (2005).

[33]L. G. Akselrud, P. Y. Zavalii, Yu. Grin, V. K. Pecharsky, B. Baumgartner, and E. Wölfel, Mater. Sci. Forum, **133–136**, 335 (1993).
[34]U. Aydemir, C. Candolfi, A. Ormeci, H. Borrmann, M. Baitinger, N. Oeschler, F. Steglich, and Yu. Grin (unpublished).
[35]K. Koepernik and H. Eschrig, Phys. Rev. B **59**, 1743 (1999).
[36]J. P. Perdew and Y. Wang, Phys. Rev. B **45**, 13244 (1992).
[37]S. Yamanaka, E. Enishi, H. Fukuoka, and M. Yasukawa, Inorg. Chem. **39**, 56 (2000).
[38]K. Moriguchi, M. Yonemura, A. Shintani, and S. Yamanaka, Phys. Rev. B **61**, 9859 (2000).
[39]J. S. Tse, T. Iitaka, T. Kume, H. Shimizu, K. Parlinski, H. Fukuoka, and S. Yamanaka, Phys. Rev. B **72**, 155441 (2005).
[40]P. Toulemonde, Ch. Adessi, X. Blase, A. San Miguel, and J. L. Tholence, Phys. Rev. B **71**, 094504 (2005).
[41]H. Fukuoka, J. Kiyoto, and S. Yamanaka, J. Solid State Chem. **175**, 237 (2003).
[42]S. Yamanaka, Dalton Trans. **39**, 1901 (2010), and references therein.
[43]K. Tanigaki, T. Shimizu, K. M. Itoh, J. Teraoka, Y. Moritomo, and S. Yamanaka, Nature Mat. **2**, 653 (2003).
[44]R. Lortz, R. Viennois, A. Petrovic, Y. Wang, P. Toulemonde, C. Meingast, M. M. Koza, H. Mutka, A. Bossak, and A. San Miguel, Phys. Rev. B **77**, 224507 (2008).
[45]W. L. McMillan, Phys. Rev. **167**, 331 (1968).
[46]D. Connetable, V. Timoshevskii, B. Masenelli, J. Beille, J. Marcus, B. Barbara, A. M. Saitta, G.-M. Rignanese, P. Melinon, S. Yamanaka, and X. Blase, Phys. Rev. Lett. **91**, 247001 (2003).
[47]Y. Noat, T. Cren, P. Toulemonde, A. San Miguel, F. Debontridder, V. Dubost, and D. Roditchev, Phys. Rev. B **81**, 104522 (2010).
[48]See, e.g., H. Lueken, in *Magnetochemie* (B.G. Teubner, Stuttgart, 1999).
[49]D. T. Morelli, T. Caillat, J. P. Fleurial, A. Borshchevsky, J. Vandersande, B. Chen, and C. Uher, Phys. Rev. B **51**, 9622 (1995).
[50]D. Mandrus, V. Keppens, B. C. Sales, and J. L. Sarrao, Phys. Rev. B **58**, 3712 (1998).
[51]R. C. Haddon, Nature (London) **378**, 249 (1995), and references therein.
[52]C. Cros, M. Pouchard, and P. Hagenmüller, J. Solid State Chem. **2**, 570 (1970).
[53]E. Gruneisen, Ann. Phys. Lpz. **16**, 530 (1933).
[54]S. Paschen, V. H. Tran, M. Baenitz, W. Carrillo-Cabrera, Yu. Grin, and F. Steglich, Phys. Rev. B **65**, 134435 (2002).